An improved numerical scheme for the approximate solution of the Parabolic Wave model

Luigi Cimorelli, Luca Cozzolino, Renata Della Morte and Domenico Pianese

ABSTRACT

In this paper, the main features and performances of a new numerical scheme, ILILPM (Improved Locally and Instantaneously Linearized Parabolic Model) are described. ILILPM is an improved version of the Parabolic and Backwater (PAB) and Linearized Parabolic Model (LPM) schemes, proposed in literature for the approximate solution of the Parabolic Wave model. The algorithm presented is able to take into account transcritical flow regime and transitions from free-surface to pressurized flow in tree-like channel networks. Due to its unconditional stability, the model allows large computational time steps, leading to very fast simulations during transients for a class of flow conditions larger than those solved by the parent schemes. The model is demonstrated by comparing its results with experimental observations and with the results provided by the numerical solution of the full De Saint-Venant equations.

Key words | channel networks, De Saint-Venant equations, hydraulic jump, numerical scheme, Parabolic Wave model, pressurized channels

Luigi Cimorelli (corresponding author)
Domenico Pianese
Dipartimento di Ingegneria Civile, Edile e Ambientale,
Università degli Studi di Napoli Federico II,
via Claudio 21,
80125 Napoli,
Italy
E-mail: *luigi.cimorelli@unina.it*

Luca Cozzolino
Renata Della Morte
Dipartimento per le Tecnologie,
Università degli Studi di Napoli Parthenope,
Centro Direzionale di Napoli,
Isola C4,
80143 Napoli,
Italy

INTRODUCTION

The modeling of unsteady flow in rivers, in open and closed conduits, or more generally in one-dimensional water bodies, is a useful tool in numerous applications, such as flooding vulnerability evaluation, sewers and drainage systems design, river training, inland navigation, and dam-break flows in narrow valleys. Water flow in one-dimensional water bodies can be described by means of the so-called De Saint-Venant equations, which are obtained under the hypothesis of gradually varying flow, hydrostatic pressure, small bed slope, negligible vertical accelerations, and uniform velocity in the cross-section (Cunge *et al.* 1980):

$$\begin{cases} \dfrac{\partial A}{\partial t} + \dfrac{\partial Q}{\partial x} = q \\ \dfrac{\partial Q}{\partial t} + \dfrac{\partial}{\partial x}\left(\dfrac{Q^2}{A} + gI_1\right) + gA\left(\dfrac{\partial z_b}{\partial x} + J\right) - gI_2 - vq = 0 \end{cases} \quad (1)$$

The meaning of the symbols used in Equation (1) is the following: x = space independent variable; t = time independent variable; $h(x,t)$ = water depth; $Q(x,t)$ = flow discharge; $A(h,x)$ = cross-section area; $q(x,t)$ = lateral inflow; $v(x,t)$ = component along x of the inflow velocity; $z_b(x)$ = bed elevation; $J(Q,h,x)$ = friction slope; g = gravity acceleration; $I_1(h,x)$ = first moment of the cross-section with respect to the free-surface level; $I_2(h,x)$ = first moment of the cross-section longitudinal variation with respect to the free-surface level (for the definitions of I_1 and I_2 see Cunge *et al.* 1980). The accurate numerical solution of the De Saint-Venant equations, which are hyperbolic in nature, can be accomplished in reasonable time, and the increased power of computers has paved the way to numerous applications such as the design of river training projects, dam-break calculation and flooding vulnerability evaluation. Together with the increase of hardware resources, the availability of sophisticated numerical methods allows the attainment of high-order accuracy, to take into account special features of the equations such as flow field and riverbed discontinuities (Cozzolino *et al.* 2011; Cimorelli *et al.* 2012b), or to consider wave propagation on dry bed for dam-break and flooding calculation (Cozzolino

doi: 10.2166/hydro.2013.130

et al. 2012). In this context, finite volume methods, spectral volume (SV) methods and discontinuous Galerkin, coupled with the upwinding of source terms (Audusse et al. 2004) and the use of approximate Riemann solvers for the calculation of numerical fluxes (Toro 1999; Bouchut 2004), have gained increasing popularity (Kutija & Murray 2007).

Despite recent advances in free-surface flow simulation, the solution of the complete De Saint-Venant system of equations is not feasible when very fast calculations are needed. Generally, explicit algorithms for the marching in time of the solution are best suited for hyperbolic systems of nonlinear equations: these algorithms are conditionally stable, and can lead to very short time steps, leading to a high computational burden. The optimal design of free-surface hydraulic systems (e.g. sewer networks, rural drainage networks, river training works) requires the hydraulic verification of the design alternatives in order to evaluate the fitness of the candidate solutions and determine if they satisfy the problem constraints (Cimorelli et al. 2012a): the computational time spent in solving the complete De Saint-Venant equations is a limiting factor that may slow down the search of optimal or nearly optimal solutions. The same happens when real-time flood simulation is considered: the numerical propagation of the flood is often accomplished in a time that is too large, and then it is useless for realistic forecast applications.

From the preceding considerations, it is clear that computationally efficient systems of equations and methods of solution should be used, where possible. In well defined circumstances, widely used mathematical alternatives to the full De Saint-Venant equations are devised by simplifying the original system of equations, and obtaining the Kinematic Wave model (Tseng 2010) or the Diffusion Wave model (Zoppou 2001). In particular, depending on the real flow conditions, when inertia terms (local accelerations, momentum fluxes) can be neglected with respect to other terms (bed slope, depth variation, friction), the full De Saint-Venant equations can be modified, obtaining the so-called Diffusion Wave model:

$$\begin{cases} \dfrac{\partial A}{\partial t} + \dfrac{\partial Q}{\partial x} = q \\ J + \dfrac{\partial}{\partial x}(h + z_b) = 0 \end{cases} \tag{2}$$

This system of equations, which is parabolic in nature, retains many of the De Saint-Venant equations' characteristics (dependence on both upstream and downstream boundary conditions, wave propagation with attenuation due to friction), but can be solved with less computational effort. For these reasons, Equation (2) is preferred for channel design optimization, real-time forecasting applications and management problems (Litrico et al. 2010).

The first and second equation of (2) can be combined obtaining the new system of equations (Cunge et al. 1980):

$$\begin{cases} \dfrac{\partial Q}{\partial t} + C\dfrac{\partial Q}{\partial x} = Cq - D\dfrac{\partial q}{\partial x} + D\dfrac{\partial^2 Q}{\partial x^2} \\ J + \dfrac{\partial}{\partial x}(h + z_b) = 0 \end{cases} \tag{3}$$

where the coefficients C and D are defined as follows:

$$D = \frac{1}{B\dfrac{\partial J}{\partial Q}}; \quad C = -\frac{\dfrac{\partial J}{\partial h}}{B\dfrac{\partial J}{\partial Q}}\left(1 - \frac{1}{B}\frac{\dfrac{\partial B}{\partial x}}{\dfrac{\partial J}{\partial h}}\right) \tag{4}$$

The meaning of the symbols used in Equations (3) and (4) is the following: $B(h, x)$ = free-surface width; $C(Q, h, x, t)$ = wave celerity; $D(Q, h, x, t)$ = wave diffusivity coefficient.

Starting from an analytical solution of the linearized convective-diffusive equation (Hayami 1951; Dooge 1973), Todini & Bossi (1986) presented the PAB (Parabolic and Backwater) model. This model was further extended to take into account lateral inflow and perturbations propagating from downstream to upstream (Franchini & Todini 1986, 1988), and was successfully applied to many real world rivers for real-time flood forecasting: Fuchun river in China, Danube river in Germany, together with Po, Arno, Tiber, Adda and Oglio rivers in Italy (Todini 1996). Existing versions of the PAB scheme are restricted to subcritical flow conditions in single open channels, while transcritical flow conditions, the pressurization of closed conduits, and wave propagation through channel networks are not allowed. A modified version of PAB, called Linearized Parabolic Model (LPM), was presented by Della Morte et al. (2001, 2006), to take into account also tree-like channel networks.

In this paper, an improved version of the cited schemes, called ILILPM (Improved Locally and Instantaneously

Linearized Parabolic Model), is presented: the proposed numerical model exploits the good properties of the original PAB scheme, namely the unconditional stability and the satisfactory accuracy, but takes into account also supercritical and transcritical flow regimes, with the formation of hydraulic jumps, the pressurization of closed conduits and the propagation of the flow through branched channel networks. The feasibility and the accuracy of the numerical scheme are proved by means of numerical test cases, also taken from the literature, which are used to define its limits and merits.

The paper is organized as follows: the basic PAB scheme is briefly recalled, before the improvements proposed are introduced. The ILILPM scheme is then demonstrated with numerical tests, before final conclusions are presented.

BASICS OF THE PARABOLIC AND BACKWATER SCHEME

We observe that the first of Equation (3) rules the propagation of the discharge Q along the channel, while the solution of the second equation is equivalent to the calculation of a steady flow water surface profile with discharge variable along the channel, under the hypothesis that the velocity head is negligible. Given the discharge distribution along the channel at the generic time level t_k, and the proper boundary conditions for h and Q, the solution of Equation (3) could be advanced in time with the following steps:

(a) The water depth profile is calculated using the second of Equation (3).
(b) The values of C and D are evaluated considering the distribution of Q and h along the channel, and are considered constant during the time interval Δt.
(c) The discharge Q is routed along the channel using the first of Equation (3), with the values of C and D calculated in point (b) above.
(d) The new discharge distribution is used as initial condition for the subsequent time level $t_{k+1} = t_k + \Delta t$.

Analytical solutions of the first of Equation (3) are available when coefficients C and D are uniform, together with the lateral inflow. In particular, when a suitable impulse response is defined, the discharge at the end of the generic reach where C and D are uniform can be evaluated by means of the convolution of input discharge and impulse response. This approach is exploited in the original version of the PAB scheme (Todini & Bossi 1986) where the one-dimensional water body is subdivided in reaches of length Δx, and the first of Equation (3) is linearized over the time increment Δt about the water surface profile in the generic space interval Δx.

With reference to the j-th reach, let x_{j-1} and $x_j = x_{j-1} + \Delta x$ be the positions of the upstream and downstream cross-sections, respectively. If the uniform lateral inflow and the input hydrograph entering the reach are discretized as a sequence of rectangular pulses, constant over the time step Δt, the flow $Q(j, k)$ across section x_j and averaged over the time interval $[(k-1)\ \Delta t,\ k\ \Delta t]$ is given by (Franchini & Todini 1988):

$$Q(j,k) = \sum_{i=1}^{k} Q(j-1,i)\,\bar{U}_{j,k-1}(k-i) + \sum_{i=1}^{k} q(j,i)\,\bar{UL}_{j,k-1}(k-i) \tag{5}$$

The function $\bar{U}_{j,k-1}(k-i)$ is the response, averaged over the time interval $[(k-1)\Delta t,\ k\ \Delta t]$, to the unit rectangular pulse entering the j-th reach during the time interval $[(i-1)\ \Delta t, i\ \Delta t]$: the subscript $(j, k-1)$ clarifies that this response is calculated at the cross-section x_j considering the wave celerity C and diffusivity D corresponding to the backwater profile at the end of the $(k-1)$-th time interval. Similarly, $\bar{UL}_{j,k-1}(k-i)$ is the response, averaged over the time interval $[(k-1)\ \Delta t, k\ \Delta t]$, to the unit uniform lateral inflow $q(j,i)$ entering the j-th reach during the time interval $[(i-1)\ \Delta t, i\ \Delta t]$. The analytical expressions of $\bar{U}(\bullet)$ and $\bar{UL}(\bullet)$ are (Todini & Bossi 1986; Franchini & Todini 1988):

$$\bar{U}(s) = \frac{IF((s+1)\Delta t) - 2IF(s\Delta t) + IF((s-1)\Delta t)}{\Delta t}, \tag{6}$$

with

$$IF(t) = \left(t - \frac{\Delta x}{C}\right) N\left(-\frac{\Delta x - Ct}{\sqrt{2Dt}}\right) + \left(t + \frac{\Delta x}{C}\right) e^{\frac{\Delta x C}{D}} N\left(-\frac{\Delta x + Ct}{\sqrt{2Dt}}\right) \tag{7}$$

and

$$\bar{U}L(s) = \frac{IFL((s+1)\Delta t) - 2IFL(s\Delta t) + IFL((s-1)\Delta t)}{\Delta t} \tag{8}$$

where (see Cimorelli (2011) for a proof)

$$IFL(t) = \frac{C}{2}\left\{t^2 - \left(t^2 + \frac{\Delta x}{C^2}\right)\left[N\left(-\frac{\Delta x - Ct}{\sqrt{2Dt}}\right) + e^{\frac{\Delta x C}{D}}N\left(-\frac{\Delta x + Ct}{\sqrt{2Dt}}\right)\right] + \frac{2\Delta x}{C}\left(t^2 - \frac{D}{C^2}\right) \times \left[N\left(-\frac{\Delta x - Ct}{\sqrt{2Dt}}\right) - e^{\frac{\Delta x C}{D}}N\left(-\frac{\Delta x + Ct}{\sqrt{2Dt}}\right)\right] + \frac{2\Delta x}{C}\sqrt{\frac{Dt}{\pi}}e^{-\frac{(\Delta x - Ct)^2}{4Dt}}\right\} \tag{9}$$

In Equations (7) and (9), $N(\bullet)$ is the *Normal Standard Distribution*.

The use of analytic solutions for the first of Equation (3) confers unconditional stability to the scheme: in this case, very large time steps are allowed, and the only limit is the level of accuracy desired. This is a clear advantage over other approaches found in the literature, where finite difference or finite volume schemes are adopted for the space discretization, and explicit algorithms are used for the marching in time of the solution (Hunter *et al.* 2005; Bates *et al.* 2010; Prestininzi *et al.* 2010): for these algorithms, the maximum time step allowed is limited by computational stability considerations.

Despite the fact that the choice of calculating the depth profile using the second of Equation (3) is congruent with the Diffusive Wave approximation, in Todini & Bossi (1986) the full energy equation

$$J + \frac{\partial}{\partial x}\left(h + z_b + \frac{Q^2}{2gA}\right) = 0, \tag{10}$$

is used. This choice can be motivated as follows:

- During steady flow conditions, the exact solution of the full de Saint-Venant equations is recovered.
- Inclusion of the velocity head is congruent with the presence of the momentum flux in the hydraulic jump equation, used when mixed flow conditions appear (see the following section).

In the original PAB method, the backwater curve, about which the first of Equation (3) is linearized at each time step, can be then evaluated solving the energy equation via the *Standard Step Method* (Henderson 1959):

$$\left[z + h + \frac{Q^2}{2gA^2}\right]_{x_{j-1}} = \left[z + h + \frac{Q^2}{2gA^2}\right]_{x_j} + \Delta x \frac{J_{x_j} + J_{x_{j-1}}}{2}; \tag{11}$$

The basic PAB scheme, as it has been described in this section, is able to cope only with free-surface subcritical conditions, in a single channel.

ILILPM: IMPROVED LOCALLY AND INSTANTANEOUSLY LINEARIZED PARABOLIC MODEL

In this section, the basic PAB method is extended in order to consider mixed regime flow and pressurization of channels in tree-like networks.

Extension to supercritical and transcritical flow regime

As discussed in the previous section, in existing versions of the PAB algorithm the water depths along the channel are evaluated solving the energy equation at the beginning of each time level, in subcritical conditions: a general method to compute water surface profile in mixed supercritical-subcritical flow regimes could provide a significant improvement to the basic PAB scheme. In this work, the water surface profile in a mixed flow regime is calculated using the algorithm described by Brunner (2010), where Equation (10) is used for supercritical and subcritical computations, separately, while the conservation of discharge Q and total momentum

$$M = \frac{Q^2}{A} + gI_1; \tag{12}$$

are imposed through hydraulic jumps. In the following, we denote with M_{sp} the total momentum corresponding to supercritical conditions, while we denote with M_{sb} the total momentum corresponding to subcritical conditions.

The surface profile algorithm used in this paper can be summarized as follows:

(a) Given a boundary condition in a downstream control section, solve Equation (10), for each pair of cross-sections, from downstream to upstream. While performing subcritical computation, the total momentum M_{sb} is evaluated for each cross-section by Equation (12). If no subcritical solution is available, then critical depth is assumed at the upstream section.
(b) Given a boundary condition in an upstream control section, M_{sp} is evaluated first. At this point, two cases are possible:
   b1. M_{sp} at the upstream control section is greater than the total momentum M_{sb} evaluated during the subcritical water surface profile computation, and then a supercritical profile computation is carried out. While computing the supercritical surface profile, the total momentum M_{sp} for each cross-section is compared with the total momentum M_{sb} computed during step *a*. If a cross-section with $M_{sp} < M_{sb}$ is met then a hydraulic jump is assumed between current and downstream cross-sections. Therefore supercritical computation is stopped and the algorithm continues from step *c*.
   b2. M_{sp} at the upstream control section is less than the total momentum M_{sb} evaluated during the subcritical water surface profile computation, and then the algorithm restarts from step *c*.
(c) Go to the first section where critical depth was located in step *a* and assume it as a new boundary condition for the supercritical profile computation. Then continue from step *b*.

The procedure depicted collocates the hydraulic jump between two computational cross-sections.

Extension to pressurized channel

In this paper, a fictitious *Preissmann Slot* (Preissmann 1961; Cunge & Wegner 1964) is introduced to extend the applicability of the model to surcharged conditions in closed conduits. The *Preissmann Slot* consists of a narrow, frictionless slot of indefinite length placed on the top of the cross-section. The slot width T_s is given by:

$$T_s = \frac{gA_f}{c^2} \tag{13}$$

where A_f is the full cross-sectional area and c is the sound celerity in water. The slot width calculated with Equation (13) is such that the increment in storage area is negligible when the water surface enters the slot, and the accuracy of the algorithm is not affected adversely. The elevation of the water in the Preissmann Slot is representative of the piezometric line elevation.

Extension from single channel to networks

The discharge immediately downstream of a network junction is computed as the sum of the discharges from the channel ends upstream. In order to relate the water depths upstream to the water depth downstream, the network junctions are modeled by the following energy balance equation:

$$\left[z + h + \frac{Q^2}{2gA^2}\right]_{up,i} = \left[z + h + \frac{Q^2}{2gA^2}\right]_{dw} + \Delta H_i\left(V_{up,i},\ V_{dw}\right) \tag{14}$$

where the subscript (up,*i*) refers to the end cross-section of *i*-th channel upstream of the junction, and dw refers to the end cross-section of the channel downstream. The last term at the right-hand side of Equation (13) represents the local head loss for the *i*-th channel upstream of the junction, and is calculated with the following formula:

$$\Delta H_i\left(V_{up,i},\ V_{dw}\right) = \begin{cases} V_{up,i} \geq V_{dw}; & \eta \cdot \dfrac{\left(V_{up,i} - V_{dw}\right)^2}{2g} \\ V_{up,i} < V_{dw}; & \eta \cdot \dfrac{\left(V_{up,i}\right)^2}{2g} \end{cases}, \tag{15}$$

where $\eta = 0.1 \div 0.3$ is a head loss coefficient.

When a junction is met during subcritical profile computations (point *a* of the water surface profile procedure), the water depth at each cross-section upstream of the junction is computed separately solving Equation (14), and the corresponding total momentum M_{sb} is evaluated.

When a junction is met during the supercritical profile computation (point $b.1$ of the water surface profile procedure), the total supercritical momentum M_{sp} is compared with the subcritical total momentum M_{sb} in each of the upstream cross-sections. If $M_{sp} > M_{sb}$ in one of the upstream cross-sections, then the flow through the junction is supercritical: in this case, the water depth immediately downstream of the junction is calculated using Equation (14), where the flow characteristics corresponding to the upstream cross-section with the greatest M_{sp} value are used.

NUMERICAL TESTS

In this section, the numerical model is demonstrated by comparing its results with experimental observations and with the results provided by the numerical solution of the full De Saint-Venant system of equations. These tests show its capability to tackle conditions such as pressurization of closed conduits and transcritical flow conditions in channel networks. Many other challenging tests have been carried out, such as the unsteady flow simulation of a network where all the conduits are pressurized, like the water distribution networks: these tests are not reported here for sake of brevity. In all the numerical tests, the slope friction J is evaluated using the Manning equation, while $g = 9.81\ \mathrm{m^2/s}$ is used for the gravity acceleration.

Irrigation channel test-case

The first numerical test refers to the simulation of an irrigation channel, where the flow discharge is regulated by means of a gate upstream. The channel, described in Wignyosukarto (1983) and Todini (1991), is $L = 4{,}500$ m long, and has a longitudinal slope $i = 0.0002$ m/m. The cross-section of the canal is trapezoidal, with bottom width $b = 2.7$ m, and its sides' inclination make an angle $\alpha = \arctan(2/3)$ with the horizontal plane. For this channel, a number of experiments have been run, and the results are available: in the case examined here, the sudden opening of the upstream gate causes the formation of a steep front wave which superposes the pre-existing steady state flow, and finally new steady state conditions are attained. The initial conditions correspond to the steady state flow with uniform discharge $Q = 2.95\ \mathrm{m^3/s}$. At time $t = 0$, the discharge is increased instantaneously in the upstream cross-section from $Q = 2.95\ \mathrm{m^3/s}$ to $Q = 6.6\ \mathrm{m^3/s}$, and then kept constant for the entire duration of the experiment. The downstream boundary condition is the critical state condition, and the roughness coefficient attributed to the canal for the calculation of the slope friction with the Manning equation is $n_M = 0.016\ \mathrm{s/m^{1/3}}$ (Todini 1991).

In Figure 1, left panel, the experimental results at distance $x = 475$ m from the upstream gate (white circles) are compared with the results supplied by ILILPM with $\Delta x = 5$ m and $\Delta t = 300$ s for the same position (continuous black line). The results show that there is overall good correspondence between numerical and experimental results,

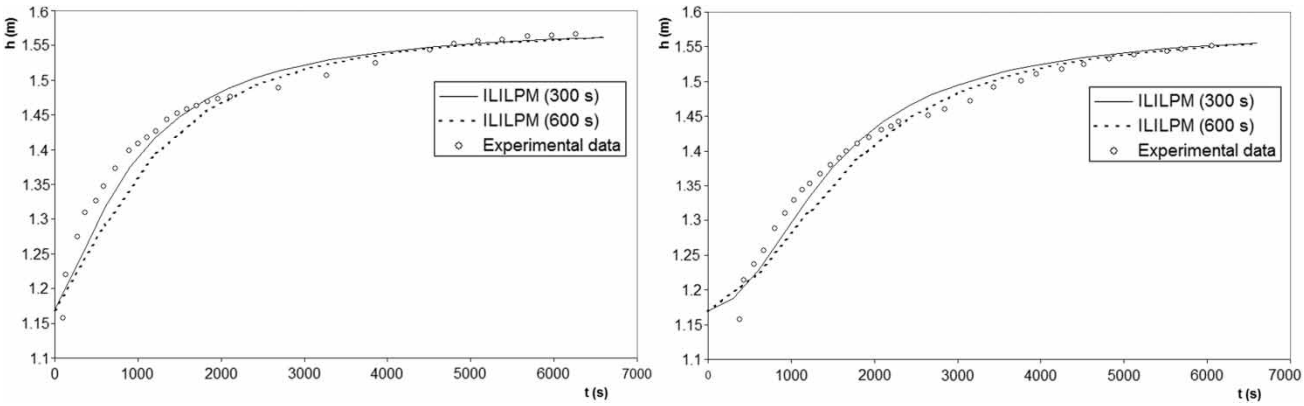

Figure 1 | Irrigation channel test-case. Comparison of experimental and numerical results at abscissas $x = 475$ m (left panel) and $x = 1{,}545$ m (right panel).

especially at the end of the experiment, when a new stationary condition is established. On the contrary, at the beginning of the experiment, immediately after the upstream gate maneuver, there is some discrepancy due to the fact that the inertia terms are not negligible: the sudden maneuver causes the formation of a steep front wave which moves downstream, and which is dissipated gradually by flow resistances. This is confirmed by the fact that in the first part of the experiment, the experimental water depth is greater than the water depth supplied by the numerical model. The same observations can be made considering the results at abscissa $x = 1{,}545$ m (Figure 1, right panel): also in this case the experimental data are better reproduced at the end of the experiment, while there is some discrepancy at the beginning.

The influence of the time discretization is greater immediately after the gate maneuver, when the time derivatives and the inertia terms are hardly negligible, while it is modest at the end of the experiment, and this is confirmed repeating the same numerical experiment with $\Delta t = 600$ s.

The same numerical test was performed by Todini & Bossi (1986) and Todini (1991) using the original version of PAB: the results obtained here show that the proposed numerical model behaves no worse than the original PAB scheme.

Moving hydraulic jump test-case

The second test aims at evaluating the ability of the proposed model to deal with situations of mixed flow, in which a hydraulic jump occurs. A rectangular channel, whose length and width are $L = 2{,}000$ m and $b = 10$ m, respectively, is composed by two reaches of equal length: the upstream reach has longitudinal slope $S_{o1} = 0.005$ m/m, while the downstream reach has slope $S_{o2} = 0.0005$ m/m. The Manning equation is used for the slope friction evaluation, and the roughness coefficient $n_M = 0.014$ s/m$^{1/3}$ is assumed. A free fall boundary condition is imposed at the downstream end of the channel. Two runs are performed, using two different upstream boundary conditions.

In the first run (Run 1), the initial conditions at $t = 0$ s coincide with the steady state conditions corresponding to the discharge $Q = 30$ m^3/s and upstream water depth $h = 0.50$ m: a stationary hydraulic jump is located at about $x = 945.75$ m from the channel inlet. Starting from $t = 0$, the upstream discharge decreases from $Q = 30$ m^3/s to $Q = 20$ m^3/s in 1,000 s, then increases to $Q = 50$ m^3/s in 1,500 s, decreasing again to $Q = 20$ m^3/s in 1,500 s. Similarly, the upstream water depth decreases from $h = 0.5$ m to 0.388 m, then increases to $h = 0.771$ m, finally decreasing again to 0.388 m. For $t > 0$, the upstream conditions are plotted in Figure 2 (Run 1). Corresponding to the boundary conditions, the hydraulic jump first moves upstream, then is pushed downstream by the raising discharge, and finally moves again upstream.

The results obtained by ILILPM using $\Delta x = 2$ m and $\Delta t = 100$ s are compared at time $t = 1{,}500$ s with those provided by a second order SV model derived by that described in Cozzolino *et al.* (2012), which solves the complete De Saint-Venant equations for rectangular cross-section channels (see Figure 3).

From the inspection of Figure 3, it is clear that ILILPM results agree very well with those supplied by the SV model,

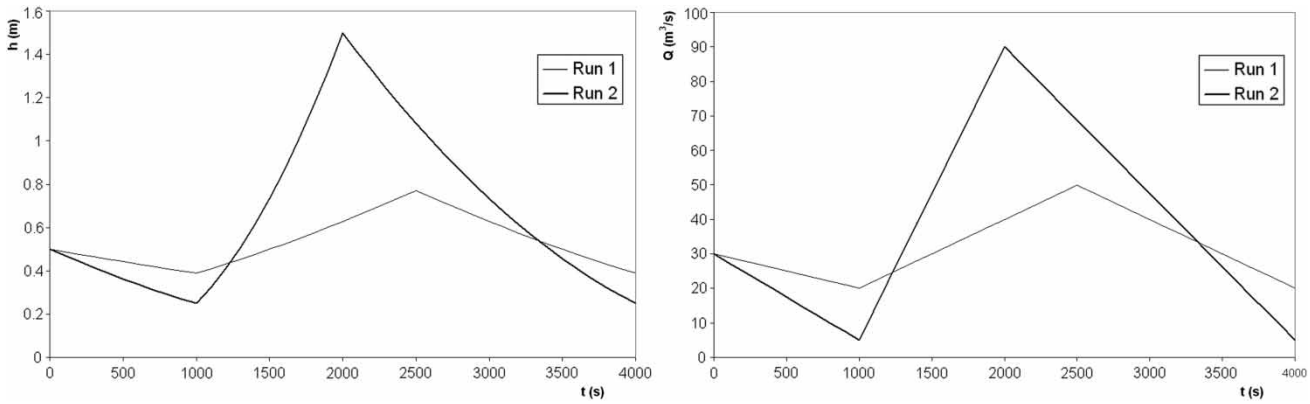

Figure 2 | Moving hydraulic jump test-case. Upstream boundary conditions for Run 1 and Run 2.

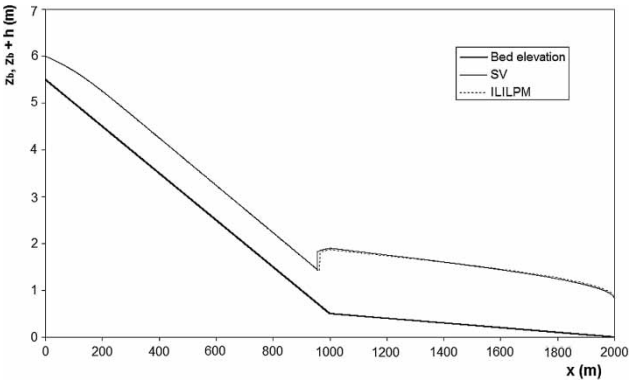

Figure 3 | Moving hydraulic jump test-case. Run 1: free-surface elevation at time $t =$ 1,500 s.

far from the discontinuity, both in supercritical and subcritical conditions. A close-up of the water surface profiles supplied by the two models in the region of the hydraulic jump is represented in Figure 4 at times $t = 1{,}500$ (left panel) and $t = 3{,}000$ s (right panel), showing a small discrepancy regarding the position of the hydraulic jump. In particular, ILILPM seems to slightly anticipate the position of the hydraulic jump, both during the movement towards downstream (raising discharge) and during the movement towards upstream (receding discharge).

In the second run (Run 2), the initial conditions coincide with those of the preceding case. Upstream boundary conditions are chosen in order to have a more steepened hydrograph: starting from $t = 0$, the upstream discharge decreases from $Q = 30\ \mathrm{m^3/s}$ to $Q = 5\ \mathrm{m^3/s}$ in 1,000 s, then increases to $Q = 90\ \mathrm{m^3/s}$ in 1,000 s, decreasing again to $Q = 5\ \mathrm{m^3/s}$ in 2,000 s. Similarly, the upstream water depth decreases from $h = 0.5$ m to 0.25 m, then increases to $h = 1.50$ m, finally decreasing to 0.25 m again. For $t > 0$, the upstream conditions are plotted in Figure 2 (Run 2).

The results obtained by ILILPM are compared again with those provided by the SV model. In particular, in Figure 5 the water surface profiles supplied by the two models are represented at times $t = 1{,}500$ (left panel) and $t = 3{,}000$ s (right panel), close to the hydraulic jump.

In the case of Run 2, the discrepancy between the position of the hydraulic jump increases, together with a greater discrepancy in the evaluation of the discontinuity strength, especially during the raising part of the flooding ($t = 1{,}500$ s). In Figure 6, the whole channel is represented at time $t = 1{,}500$ s for Run 2: it is apparent that the De Saint-Venant equations develop a wave moving downstream whose front steepens, due to the sudden increase of the discharge upstream; this effect is not reproduced by the Parabolic Wave model, solved with ILILPM.

Actually, also when starting from smooth initial conditions, the De Saint-Venant equations have solutions that may exhibit special features such as moving discontinuities, whose celerity and strength are related by means of the Rankine-Hugoniot condition (LeVeque 1992), and this mechanism is incorporated in the SV model. On the contrary, ILILPM is based on the ability to perform, at each time level, a water surface profile in mixed flow conditions: of course, the position of the hydraulic jump obtained in this way is rigorous only in the case of stationary conditions. This explains why the discrepancy between the hydraulic jump positions supplied by ILILPM and SV model increases when the input hydrograph steepens: in these conditions, the flow rapidly changing upstream promotes oscillation of the

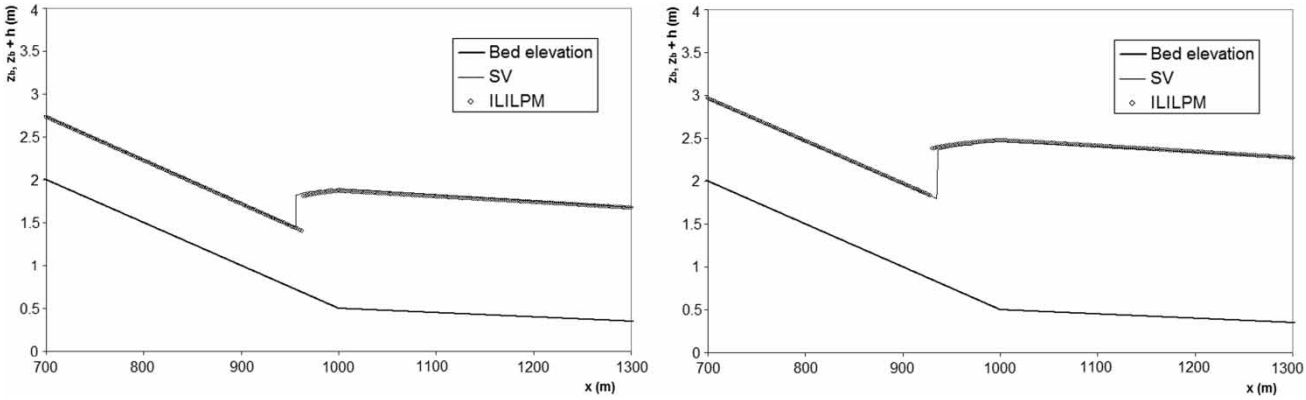

Figure 4 | Moving hydraulic jump test-case. Run 1: free-surface elevation at times $t = 1{,}500$ s (left panel) and $t = 3{,}000$ s (right panel), close-up at the hydraulic jump.

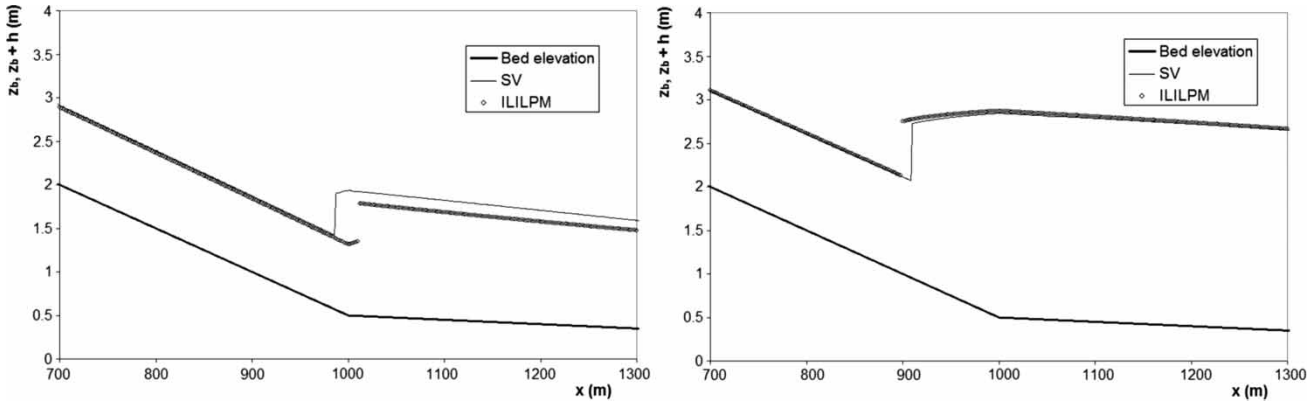

Figure 5 | Moving hydraulic jump test-case. Run 2: free-surface elevation at times $t = 1{,}500$ s (left panel) and $t = 3{,}000$ s (right panel), close-up at the hydraulic jump.

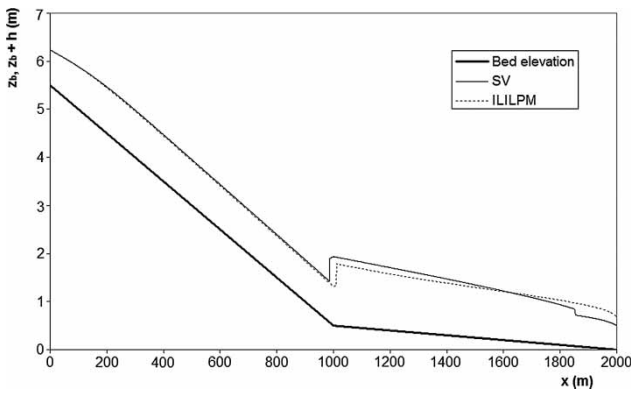

Figure 6 | Moving hydraulic jump test-case. Run 2: free-surface elevation at times $t = 1{,}500$ s in the downstream part of the channel.

discontinuity position, and this movement is not captured by the ILILPM model. Finally, from results of Run 1, it seems clear that when discontinuities are present in the flow field, ILILPM is able to approximate satisfactorily the position and the strength of such discontinuities if these are moving slowly: this ability is lost in the case of fast transients.

The maximum water depth attained during the unsteady flow phenomenon constitutes important design information, in order to evaluate flooding vulnerability in open channels or the possibility of pressurization in closed conduits. In Figure 7, a comparison is made between the time-graphs of the water depth supplied by SV and ILILPM models at locations around and inside the region where the hydraulic jump develops.

In the left panel of Figure 7, the results for Run 1 are reported at locations $x = 900$ m, $x = 960$ m and $x = 1{,}020$. From the inspection of the figure, it is apparent that at location $x = 900$ m, where the flow remains supercritical during the entire simulation, the results supplied by SV and ILILPM are very close. The comparison of the results at location $x = 1{,}020$ m, where the flow remains subcritical

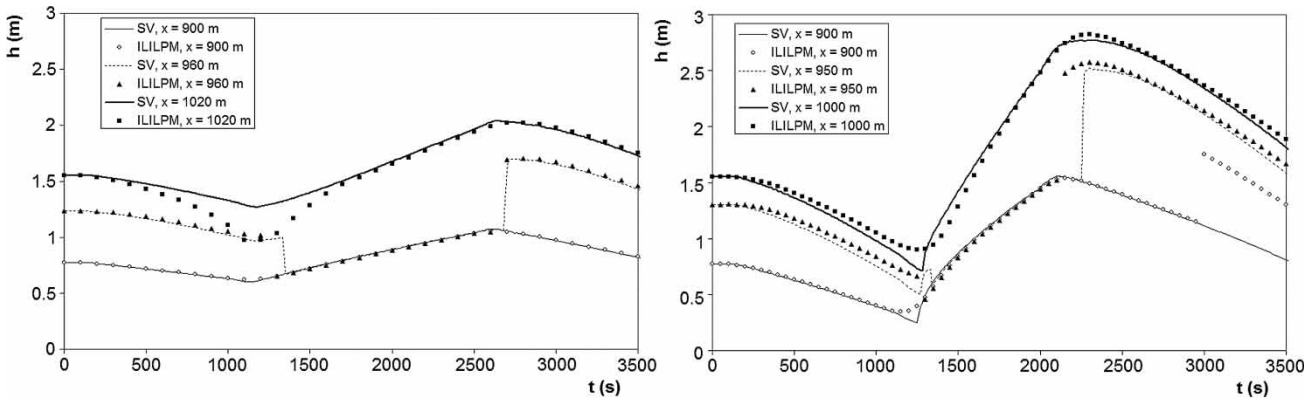

Figure 7 | Moving hydraulic jump test-case. Run 1: time-graphs of the water depth at locations $x = 900$ m, $x = 960$ m and $x = 1{,}020$ m (left panel). Run 2: time-graphs of the water depth at locations $x = 900$ m, $x = 950$ m and $x = 1{,}000$ m (right panel).

during the simulation, is less satisfactory: nonetheless, the value of the peak water depth is almost the same for the two models. At location $x = 960$ m, the flow passes from subcritical to supercritical, and *vice versa*, following the moving hydraulic jump: surprisingly, also in this case the correspondence of the peak water level is very good, while the correspondence of the time arrival and the strength of the hydraulic jump is not unsatisfactory.

In the right panel of Figure 7, the results of Run 2 are plotted. At the location $x = 950$ m, where the flow reverts from subcritical to supercritical and *vice versa*, an overall correspondence of the results supplied by the two models is observed, especially with reference to the peak water depth. The correspondence between the results supplied by the two models at location $x = 900$ m and $x = 1{,}000$ m is much less satisfactory: actually, ILILPM exaggerates the celerity of hydraulic jump movement towards upstream and downstream, respectively. Nonetheless, the correspondence of the peak water depths supplied by the two models is satisfactory at $x = 1{,}000$ m.

The superior envelopes of water depths profiles supplied by SV and ILILPM models are plotted in Figure 8 for both Runs 1 and 2, respectively. Despite the fact that the instantaneous water depths calculated with the two models can be very different, from inspection of Figure 8 we can deduce that the maximum water depths are very similar: this is confirmed by the fact that the average error between the envelope water depths supplied by ILILPM and SV is 1.6% for Run 1, and 1.2% for Run 2.

The results of the numerical test support the conclusion that ILILPM is a viable and efficient alternative to the solution of the full De Saint-Venant system, including when discontinuities such as hydraulic jumps are present in the flow field, if attention of the modeler is paid to important design parameters such as the peak water level. As expected, less satisfactory results are obtained with reference to the arrival time of discontinuities.

Pressurization of a channel test-case

The purpose of the third test is to evaluate the effectiveness of the model to cope with situations where a transition from free-surface flow to pressurized flow occurs. For this test, a closed conduit consisting of three consecutive reaches is considered: each channel is $L = 500$ m long, with circular cross-section, diameter $D = 1.00$ m and Manning roughness coefficient $n_M = 0.00125\ \mathrm{s/m^{1/3}}$. The three reaches have bed slope $S_{o1} = 0.040$ m/m, $S_{o2} = 0.001$ m/m and $S_{o3} = 0.030$ m/m, respectively, from upstream to downstream, and the bottom elevation at the upstream end of the conduit is $z_b = 100$ m. The initial conditions coincide with the steady state corresponding to the discharge $Q = 0.010\ \mathrm{m^3/s}$: starting from these initial conditions, upstream discharge increases linearly in 3,600 s to $Q = 2.00\ \mathrm{m^3/s}$, and then decreases again to $Q = 0.010\ \mathrm{m^3/s}$ in 3,600 s and critical depth was assumed as the upstream boundary condition. During the numerical experiment, the downstream boundary condition is constant: in particular, the water depth at the downstream end of the conduit is taken equal to $h = 0.500$ m.

The sudden discharge increase causes the pressurization of the second reach, due to its small longitudinal slope. In

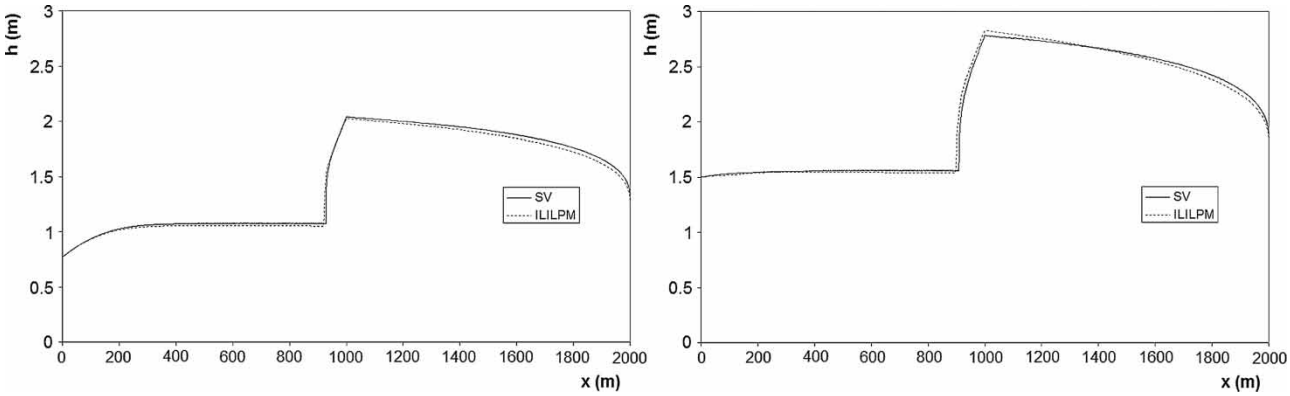

Figure 8 | Moving hydraulic jump test-case. Superior envelopes of the water depths for Run 1 (left panel) and Run 2 (right panel).

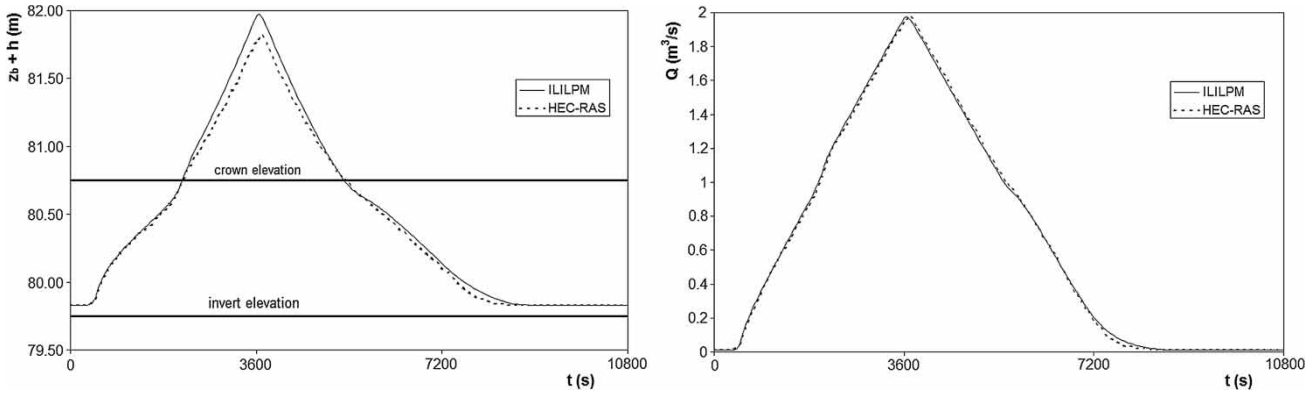

Figure 9 | Pressurization of a channel test-case. Reach 2: piezometric line (left panel) and discharge (right panel).

Figure 9, the results obtained by ILILPM with $\Delta x = 10$ m and $\Delta t = 60$ s for a cross-section at distance $x = 750$ m from the upstream end of the channel are compared with those provided by HEC-RAS 4.1, which solves the full De Saint-Venant system and employs the Preissmann slot to take into account pressurization.

It is apparent that the ILILPM model, despite the fact that is based on the parabolic wave simplification, is able to reproduce reasonably the pressurization results obtained with HEC-RAS. The starting time and the duration of the pressurization condition supplied by the ILILPM model coincide with those supplied by HEC-RAS (Figure 9, left panel), while the pressure peak supplied by ILILPM is slightly greater: this discrepancy is attributed to the low accuracy attained by HEC-RAS during pressurized flow calculations, due to stability issues. In Figure 9, right panel, the time-discharge graph is plotted for the two models, showing how the results are fully consistent.

In Figure 10, the same comparison is made for a cross-section at a distance of $x = 1{,}250$ m from the upstream end of the channel, in the third reach, where again free-surface flow is present, due to the increased bed slope. It is clear, also for this section, that ILILPM supplies results very similar to those supplied by HEC-RAS: the pressurization in the second reach does not affect adversely the flow simulation in the end reach, considering both the water depth and discharge evaluation.

Zhang (2005) network test-case

This test-case was presented first by Zhang (2005), and refers to a very simple network, consisting of three rectangular channels, forming a Y. The three channels have longitudinal slope $S_o = 0.0002$ m/m, length $L = 5{,}000$ m, and are characterized by a Manning roughness coefficient $n_M = 0.025$ s/m$^{1/3}$. The two upstream channels have width $B = 50$ m,

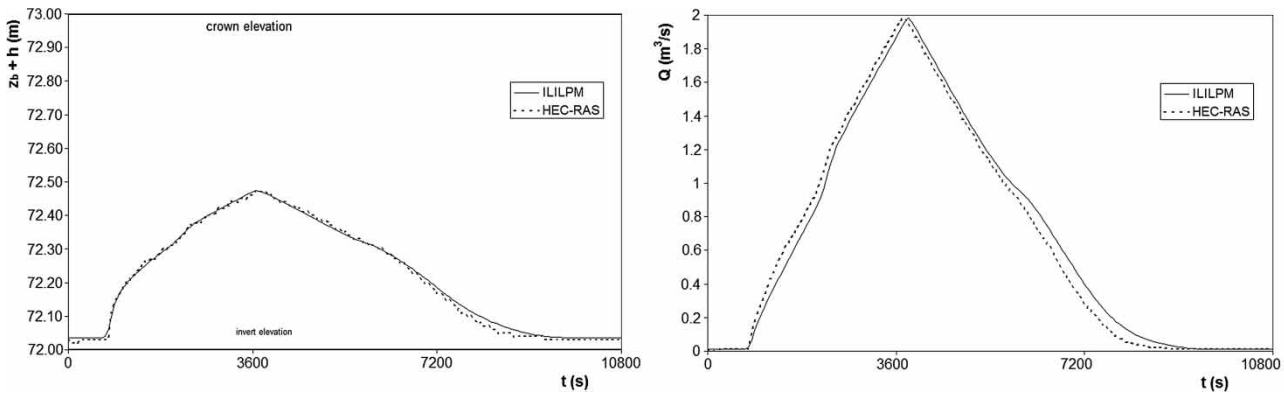

Figure 10 | Pressurization of a channel test-case. Reach 3: piezometric line (left panel) and discharge (right panel).

while the downstream channel has width $B = 100$ m. Initial conditions at $t = 0$ correspond to uniform flow conditions, with discharge flow $Q = 50\ m^3/s$ in the two channels upstream, and $Q = 100\ m^3/s$ in the channel downstream. Starting from $t = 0$, a triangular hydrograph enters the two upstream channels upstream, and the input discharge increases in both channels from $Q = 50\ m^3/s$ to $Q = 150\ m^3/s$ in 2,000 s, then decreases again to $Q = 50\ m^3/s$ in 2,000 s.

The results supplied by ILILPM with $\Delta x = 500$ m and $\Delta t = 100$ s for the cross-section at distance $l = 1{,}000$ m from the downstream end of the network are plotted in Figure 11. In the same figure, the ILILPM results are compared with those obtained with two models for the solution of the complete De Saint-Venant equations, namely the finite difference model HEC-RAS and the finite element model by Zhang (2005). From inspection of Figure 11, it is apparent that significant differences can be devised between the different models. Apparently, ILILPM anticipates the peak discharge with respect to the model by Zhang (2005), and this causes the flattening of the hydrograph: in particular, the peak discharge supplied by the Zhang (2005) model is greater than the peak supplied by ILILPM.

It seems that this effect cannot be attributed to the mathematical differences between the De Saint-Venant equations, solved by the finite element model by Zhang (2005) and the Parabolic Wave model, solved by ILILPM: actually, when the finite difference model HEC-RAS, which solves the full De Saint-Venant equations, is applied to the same test-case, its results are quite similar to those supplied by ILILPM. At the moment, there is no clear explanation for the discrepancy between the model by Zhang (2005) on one side, and HEC-RAS and ILILPM on the other: this will be the object of future research.

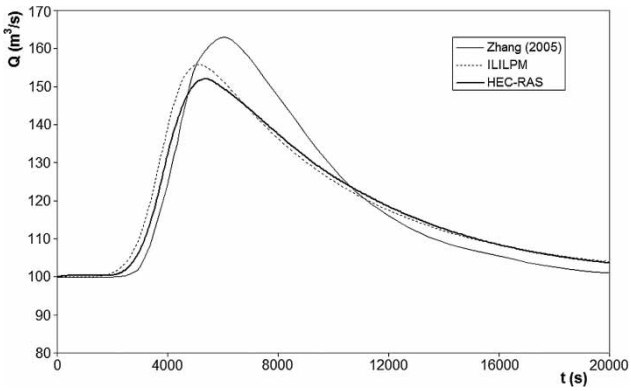

Figure 11 | Zhang (2005) test-case. Time graph of the discharge at $l = 1{,}000$ m from the downstream end of the network.

CONCLUSIONS

When fast transients are considered, the full De Saint-Venant system of equations is the first choice for modeling the flow in one-dimensional water bodies, and its numerical solution should be accomplished in practical applications. Conversely, when inertia terms are negligible, the Parabolic Wave model, which is a simplification of the De Saint-Venant system, is an attractive alternative, due to its computational efficiency. In this paper, a novel numerical scheme for the approximate solution of the Parabolic Wave model, called ILILPM, has been presented: the proposed scheme is an improvement of existing numerical models, PAB (Todini & Bossi 1986) and LPM (Della Morte *et al.* 2001, 2006), and allows the user to take into account pressurization of closed conduits and flow discontinuities. The numerical scheme has been demonstrated by comparing its results with experimental observations and with the results provided by the numerical solution of the full De Saint-Venant system of equations: the test-cases show that ILILPM is able to reproduce reasonably the results of slow transients in open channel networks and closed conduits, and also in the presence of flow discontinuities such as hydraulic jumps. While at a given instant the accuracy can be insufficient during fast transients, ILILPM is able to capture surprisingly well the maximum value of water depths also for these cases. The encouraging results obtained demonstrate how ILILPM is a promising tool for the fast simulation of drainage networks, especially in the case of real-time flood forecasting or when the optimization of sewers and drainage networks design is faced.

REFERENCES

Audusse, E., Bouchut, F., Bristeau, M.-O., Klein, R. & Perthame, B. 2004 A fast and stable well-balanced scheme with hydrostatic reconstruction for shallow water flows. *SIAM J. Sci. Comput.* **25** (6), 2050–2065.

Bates, P. D., Horritt, M. S. & Fewtrell, T. J. 2010 A simple inertial formulation of the shallow water equations for efficient two-dimensional flood inundation modelling. *J. Hydrol.* **387** (1–2), 33–45.

Bouchut, F. 2004 *Nonlinear Stability of Finite Volume Methods for Hyperbolic Conservation Laws and Well-Balanced Schemes for Sources. Frontiers in Mathematics*. Birkhäuser Verlag, Basel.

Brunner, G. W. 2010 *HEC-RAS, River Analysis System Hydraulic Reference Manual, Version 4.1*. U.S. Army Corps of Engineers-Hydrologic Engineering Center, Davis, CA.

Cimorelli, L. 2011 Modellazione e Progettazione Ottimizzata delle Reti di Drenaggio, Ph.D. Thesis, Federico II Open Archive.

Cimorelli, L., Cozzolino, L., Covelli, C., Mucherino, C., Palumbo, A. & Pianese, D. 2012a Optimal design of rural drainage networks. *ASCE J. Irrig. Drain. Eng.* **139** (2), 137–144.

Cimorelli, L., Covelli, C., Cozzolino, L., Della Morte, R. & Pianese, D. 2012b A derivative recovery spectral volume model for the analysis of constituents transport in one-dimensional flows. *J. Math. Syst. Sci.* **2**, 334–340.

Cozzolino, L., Della Morte, R., Covelli, C., Del Giudice, G. & Pianese, D. 2011 Numerical solution of the discontinuous-bottom shallow-water equations with hydrostatic pressure distribution at the step. *Adv. Water Resour.* **34** (11), 1413–1426.

Cozzolino, L., Della Morte, R., Del Giudice, G., Palumbo, A. & Pianese, D. 2012 A well-balanced spectral volume scheme with the wetting–drying property for the shallow-water equations. *J. Hydroinf.* **14** (3), 745–760.

Cunge, J. A. & Wegner, M. 1964 Intégration numérique des equations d'écoulement de Barré de Saint-Venant par un schéma implicite de differences finies. *La Houille Blanche* **1**, 33–38.

Cunge, J. A., Holly Jr., F. M. & Verwey, A. 1980 *Practical Aspects of Computational River Hydraulics*. Pitman Publishing Limited, London.

Della Morte, R., Iavarone, V., Mucherino, C. & Pianese, D. 2006 Applicazione di un modello idraulico semplificato per l'analisi dei fenomeni di moto vario nelle reti di drenaggio. *L'Acqua* **2**, 37–44.

Della Morte, R., Iavarone, V. & Pianese, D. 2001 Evaluation of Maximum Flow Depths and Discharges in Drainage Network by a Simplified Model Coupled to a Variational Approach. In: *Proceedings of the 29th IAHR Congress – Theme D2*, Beijing, China, 16–21 September, pp. 689–696.

Dooge, J. C. 1973 The linear theory of hydrologic systems. *US Dept. Agric. Tech. Bull.* No. 1468, Washington D.C.

Franchini, M. & Todini, E. 1986 BAP. Uno schema di calcolo per la simulazione di perturbazioni propagantesi contro corrente in canali a pelo libero. *L'Energia Elettrica* **63** (6), 247–250.

Franchini, M. & Todini, E. 1988 PABL: A parabolic and Backwater scheme with lateral inflow and outflow. Fifth IAHR international symposium on stochastic hydraulics, Birmingham, August 1988.

Hayami, S. 1951 *On the Propagation of Flood Waves*. Disaster Prevention Research Institute, Kyoto University, Kyoto.

Henderson, F. M. 1959 *Open Channel Flow*. Macmillan Company, New York.

Hunter, N. M., Horritt, M. S., Bates, P. D., Wilson, M. D. & Werner, M. G. F. 2005 Adaptive time step solution for raster-based storage cell model. *Adv. Water Resour.* **28** (9), 975–991.

Kutija, V. & Murray, M. G. 2007 An object-oriented approach to the modeling of free-surface flows. *J. Hydroinf.* **9** (2), 81–94.

LeVeque, R. J. 1992 *Numerical Methods for Conservation Laws*. Birkhäuser Verlag, Berlin.

Litrico, X., Pomet, J.-B. & Guinot, V. 2010 Simplified nonlinear modeling of river flow routing. *Adv. Water Resour.* **33**, 1015–1023.

Preissmann, A. 1961 Propagation des intumescences dans les canaux et riviers. *1er Congrès d'Association Française de Calcul*, Grenoble, France, pp. 433–442.

Prestininzi, P., Di Baldassarre, G., Schumann, G. & Bates, P. D. 2010 Selecting the appropriate hydraulic model structure using low-resolution satellite imagery. *Adv. Water Resour.* **34** (1), 38–46.

Todini, E. 1991 Hydraulic and hydrologic flow routing schemes. In: *Recent Advances in the Modelling of Hydrologic Systems – Proceedings of the NATO Advanced Studies Institute* (D. S. Bowler, ed.). Kluwer Academic Publishers, Dordrecht, pp. 389–405.

Todini, E. 1996 The ARNO rainfall-runoff model. *J. Hydrol.* **175**, 339–382.

Todini, E. & Bossi, A. 1986 PAB (Parabolic and Backwater), an unconditionally stable flood routing scheme particularly suited for real time forecasting and control. *J. Hydraul. Res.* **24** (5), 405–424.

Toro, E. F. 1999 *Riemann Solvers and Numerical Methods for Fluid Dynamics. A Practical Introduction*. Birkhäuser Verlag, Berlin.

Tseng, M.-H. 2010 Kinematic wave computation using an efficient implicit method. *J. Hydroinf.* **12** (3), 329–338.

Wignyosukarto, B. 1983 Ecoulement transitoire en canal – Application à la regulation – Rapport de D. E. A. de Mecanique des Fluides. Ecole Nationale Superieure de Grenoble.

Zhang, Y. 2005 Simulation of open channel network flows using finite element approach. *Commun. Nonlinear Sci. Numer. Simul.* **10** (5), 467–478.

Zoppou, C. 2001 Review of urban storm water models. *Environ. Modell. Softw.* **16** (3), 195–231.

First received 2 August 2012; accepted in revised form 23 January 2013. Available online 14 February 2013